Journal of Global Positioning Systems (2026)
Vol. 22,Issue 2:239-254
DOI:10.5081/jpgps.22.2.239

Investigation of Ionospheric Constraint Strategies in Multi-frequency and Multi-GNSS PPP-RTK

Zhihan Sun[1,2], Wang Gao[1,2]✉, Shuguo Pan[1,2], Qing Zhao[1,2], Xianlu Tao[1,2]

[1] School of Instrument Science and Engineering, Southeast University, Nanjing 210096, China;

[2] State Key Laboratory of Comprehensive PNT Network and Equipment Technology, Southeast University, Nanjing 210096, China

✉ The corresponding author, gaow@seu.edu.cn

Abstract: The performance improvement of precise point positioning real-time kinematic (PPP-RTK) relies on external ionospheric information. Its enhancement effectiveness is governed not only by the accuracy of service-side ionospheric products, but also by the user-side constraint strategy. This study establishes a unified experimental framework to investigate the applicability of three established ionospheric constraint strategies under the coupled effects of service-side product precision and user-side observation redundancy in a multi-frequency multi-global navigation satellite system (GNSS) PPP-RTK. Experimental results show that, compared with the ionosphere-float and ionosphere-fixed strategies, the ionosphere-weighted strategy reduces the three-dimensional positioning error by 4%-57% and 15%-60%, respectively. On this basis, the influence of observation conditions on positioning performance is further analyzed. When the BeiDou navigation satellite system (BDS) observation model is extended from dual-frequency to triple-frequency, the horizontal positioning accuracy is improved by 4%-17%; when the BDS/global positioning system (GPS) model is further extended to a triple-frequency BDS/GPS/Galileo navigation satellite system (Galileo) model, the horizontal positioning accuracy is improved by 11%-46%, indicating that multi-frequency multi-GNSS observations are beneficial for improving model redundancy and positioning performance. In addition, the adaptability analysis of the ionosphere-weighted strategy to constraint strength under different observation conditions shows that the ambiguity fixing rate reaches its optimum when the constraint strength matches the actual error level of products. Under high-redundancy observation conditions, overly strong constraints aggravate the propagation of product biases, whereas conservative constraints lead to relatively limited performance loss. These results indicate that, for ionospheric constraint strategies in multi-frequency multi-GNSS PPP-RTK, greater attention should be paid to the reliable precision boundary of service-side products, while excessively strong constraints on external atmospheric corrections should be avoided.

Keywords: PPP-RTK; ionospheric constraints; ionosphere-weighted; multi-frequency multi-GNSS; observation redundancy

1. Introduction

Precise point positioning (PPP) can achieve decimeter- to centimeter-level positioning accuracy with the aid of high-quality products, such as precise satellite orbits and clock corrections (Zumberge et al., 1997). However, its convergence performance is constrained by the coupling between carrier-phase ambiguities and atmospheric errors (Xiao et al., 2024). Precise point positioning real-time kinematic (PPP-RTK) introduces regional augmentation information into the PPP framework and applies precise satellite products, bias corrections, and regional atmospheric corrections to user-side estimation, thereby providing an effective approach for rapid and high-precision positioning (Wabbena et al., 2005; B. Zhang et al., 2011). Among the various augmentation products, the accuracy and reliability of ionospheric correction products directly affect ambiguity fixing efficiency, parameter separability, and final positioning performance (P. J. Teunissen et al., 2010). Therefore, how to fully and properly exploit the ionospheric augmentation information provided by the service-side (X. Zhang et al., 2022; Wang et al., 2023) has become one of the key issues in PPP-RTK research.

To address this issue, research has gradually evolved along two complementary directions, namely the generation of reliable augmentation information at the service-side and the adaptive use of such information at the user-side. On the one hand, the service-side focuses on extracting high-precision ionospheric delays from regional reference station networks and further generating regional correction

products that can be directly applied by users (X. Li et al., 2023; W. Zhang et al., 2024). On the other hand, the user-side focuses on how to effectively incorporate external ionospheric information into the PPP-RTK model and achieve a dynamic balance among model errors, product precision, and observation redundancy (Odijk et al., 2000; Zha et al., 2021). Existing studies have shown that external ionospheric information can significantly improve the convergence speed and ambiguity fixing performance of PPP-RTK (Psychas et al., 2019; Psychas & Verhagen, 2020). However, the resulting enhancement effectiveness depends not only on the accuracy of the service-side products themselves, but also on the way such information is constrained and utilized at the user-side. In other words, the performance improvement of PPP-RTK is jointly governed by two key factors: first, whether the service-side can provide ionospheric products with reliable accuracy and properly characterized uncertainty; and second, whether the user-side can select an appropriate constraint strategy according to product quality and its own observation conditions, so as to balance external prior information and self-estimation capability.

Regarding the first issue, the research focus at the service-side has gradually evolved from high-precision modeling of ionospheric delays to the joint generation of correction values and their uncertainty information for high-reliability applications. One line of research starts from spatial interpolation models and develops new interpolation methods based on the spatial correlation structure among reference stations to improve the accuracy of service-side products (Dai et al., 2001; Song et al., 2016). Another line of research addresses this issue from the perspective of quality assessment, where data-driven evaluations of ionospheric correction errors are conducted through strategies such as cross-validation and external residual analysis, and then transformed into precision information directly usable at the user-side, thereby providing more practical stochastic information descriptions for user positioning (P. Li et al., 2022; Huang et al., 2025; Du et al., 2026). However, the uncertainty of service-side products remains a statistical representation under regional network conditions, and may still deviate from the instantaneous errors at a specific user location and epoch. Therefore, the user terminal still needs to adaptively utilize external augmentation information in combination with its own observations and estimation status.

At the user-side, a variety of typical constraint strategies have been developed for exploiting external ionospheric augmentation information. Early studies mainly focused on the practical impact of different constraint strengths on PPP-RTK performance. From an application perspective, these studies systematically analyzed how changes in the variance assigned to external ionospheric constraints affect convergence speed, ambiguity fixing rate, and positioning accuracy, showing that the effectiveness of user-side utilization of augmentation information is highly sensitive to constraint strength (X. Zhang et al., 2022). Subsequent studies further characterized this phenomenon from a theoretical perspective. Based on the mean squared error (MSE) criterion, (P. J. G. Teunissen & Khodabandeh, 2021) derived the conditions under which the ionosphere-weighted strategy outperforms the ionosphere-fixed and ionosphere-float strategies, thereby providing quantitative criteria for the applicability boundaries of different constraint approaches and demonstrating that user-side ionospheric processing is essentially a matching problem between external product errors and the terminal stochastic model. On this basis, further studies have attempted to move beyond the traditional statistical constraint framework based on variance description. Of particular relevance, work in the real-time kinematic (RTK) field has transformed ionospheric constraints from variance-based stochastic regulation into inequality constraints and solved them within a quadratic programming framework (Mi et al., 2026), thereby providing a new mathematical perspective for the utilization of ionospheric augmentation information. However, under multi-frequency multi-global navigation satellite system (GNSS) PPP-RTK conditions, where observation redundancy is significantly enhanced, the performance differences among different constraint strategies under different observation conditions still require further verification. In particular, when the precision boundary of service-side products is fixed, the adaptability of user-side ionosphere-fixed, ionosphere-weighted, and ionosphere-float strategies still lacks systematic experimental evaluation.

In view of this, this study investigates user-side constraint strategies for ionospheric augmentation information in a multi-frequency multi-GNSS PPP-RTK scenario. At the service-side, ionospheric corrections and their associated precision information are generated for user application. At the user-side, three typical strategies, namely ionosphere-fixed, ionosphere-weighted, and ionosphere-float, are constructed and comparatively analyzed in terms of positioning error, convergence performance, and ambiguity fixing. Furthermore, by considering the enhanced observation redundancy under multi-frequency multi-GNSS conditions, the effects of the service-side product precision boundary and the user-side model redundancy on the applicability of different constraint strategies are discussed.

This study focuses on the applicability of established constraint strategies under the coupled effects of service-side product precision and user-side observation redundancy in multi-frequency multi-GNSS PPP-RTK. The main contributions of this study are threefold. First, three strategies are formulated within a unified user-side framework, allowing their performance differences to be evaluated under consistent service-side products and observation conditions. Second, the joint influence of product precision and user-side model redundancy is

systematically investigated by combining different reference-network configurations with different multi-frequency and multi-GNSS observation models, thereby clarifying how observation redundancy changes the user's dependence on external ionospheric information. Third, the sensitivity of the ionosphere-weighted strategy to constraint strength is quantified, revealing the relationship among product-error level, constraint strength, ambiguity fixing, and positioning performance. These analyses provide a practical basis for selecting and potentially adapting ionospheric constraint strength according to product reliability and user-side observation conditions.

2. Methods

This section introduces the atmospheric delay processing methods in PPP-RTK from both the service-side and user-side perspectives, and further presents the three classical atmospheric constraint strategies adopted at the user-side.

2.1 Service-side processing

For the pseudorange and carrier-phase observations at frequency i from reference station r to satellite s, the undifferenced and uncombined observed-minus-computed (OMC) equations can be written as:

$$\begin{cases} E\left(\Delta P_{r,i}^{s}\right)=\mathbf{c}_{r}^{s}\cdot\Delta\mathbf{x}_{r}+c\left(dt_{r}-dt^{s}\right)+g_{r}^{s}T_{r}^{s}+\mu_{i}I_{r,i}^{s}+b_{r,i}-b_{i}^{s} \\ E\left(\Delta\Phi_{r,i}^{s}\right)=\mathbf{c}_{r}^{s}\cdot\Delta\mathbf{x}_{r}+c\left(dt_{r}-dt^{s}\right)+g_{r}^{s}T_{r}^{s}-\mu_{i}I_{r,i}^{s}+B_{r,i}-B_{i}^{s}+\lambda_{i}N_{r,i}^{s} \end{cases} \quad (1)$$

where $E(.)$ denotes the expectation operator; $\Delta P_{r,i}^{s}$ and $\Delta\Phi_{r,i}^{s}$ denote the OMC values of pseudorange and carrier-phase observations, respectively; $\Delta\mathbf{x}_{r}$ is the coordinate correction vector of the reference station; $\mathbf{c}_{r}^{s}$ is the line-of-sight unit vector from receiver to satellite; c is the speed of light; dt_{r} and dt^{s} denote the receiver clock offset and satellite clock offset, respectively; T_{r}^{s} denotes the zenith tropospheric delay parameter; g_{r}^{s} is the tropospheric mapping function; $I_{r,i}^{s}$ denotes the first-order slant ionospheric delay at frequency i; $\mu_{i}=f_{1}^{2}/f_{i}^{2}$ is the ionospheric frequency scaling factor; $b_{r,i}$ and b_{i}^{s} denote the receiver and satellite pseudorange hardware biases, respectively; $B_{r,i}$ and B_{i}^{s} denote the receiver and satellite carrier phase hardware biases, respectively; $\lambda_{i}=c/f_{i}$ is the wavelength of the i-th frequency; and $N_{r,i}^{s}$ is the integer ambiguity parameter.

Since Eq. (1) is rank-deficient, the original code biases need to be re-parameterized in order to construct an estimable parameter. Two commonly used linear combination schemes are the ionosphere-free (IF) bias and the geometry-free (GF) bias (Montenbruck et al., 2014). Let the two reference frequencies be f_{1} and f_{2}, with the corresponding ionospheric frequency coefficients denoted by μ_{1} and μ_{2}, respectively. For the dual-frequency pseudorange hardware bias vector at either the receiver or the satellite $\mathbf{b}=\begin{bmatrix}b_{1} & b_{2}\end{bmatrix}^{\mathrm{T}}$, the IF bias, GF bias, and differential code bias (DCB) can be uniformly expressed as:

$$\begin{bmatrix} b_{\mathrm{IF}} \\ b_{\mathrm{GF}} \\ D_{\mathrm{DCB}} \end{bmatrix}=\begin{bmatrix} \dfrac{\mu_{2}}{\mu_{2}-\mu_{1}} & -\dfrac{\mu_{1}}{\mu_{2}-\mu_{1}} \\ -\dfrac{1}{\mu_{2}-\mu_{1}} & \dfrac{1}{\mu_{2}-\mu_{1}} \\ -1 & 1 \end{bmatrix}\mathbf{b},\mathbf{b}\in\left\{\begin{bmatrix} b_{1}^{s} \\ b_{2}^{s} \end{bmatrix},\begin{bmatrix} b_{r,1} \\ b_{r,2} \end{bmatrix}\right\} \quad (2)$$

When $\mathbf{b}=\begin{bmatrix}b_{1}^{s} & b_{2}^{s}\end{bmatrix}^{\mathrm{T}}$, b_{IF}^{s}, b_{GF}^{s}, and D_{DCB}^{s} denote the corresponding IF bias, GF bias, and DCB at the satellite side, respectively; when $\mathbf{b}=\begin{bmatrix}b_{r,1} & b_{r,2}\end{bmatrix}^{\mathrm{T}}$, $b_{r,IF}$, $b_{r,GF}$, and D_{DCB}^{r} denote the corresponding quantities at the receiver side. It follows from Eq. (2) that the pseudorange hardware bias at any frequency can be expressed as a linear combination of the IF and GF biases. Substituting this relation into the pseudorange observation equation in Eq. (1), the ionosphere-related terms can be rearranged as:

$$\mu_{i}I_{r}^{s}+b_{r,i}-b_{i}^{s}=\left(b_{r,\mathrm{IF}}-b_{\mathrm{IF}}^{s}\right)+\mu_{i}\left(I_{r}^{s}+b_{r,\mathrm{GF}}-b_{\mathrm{GF}}^{s}\right) \quad (3)$$

Equation (3) indicates that the IF bias appears as a frequency-independent constant term, whereas the GF bias shares the same frequency-scaling structure as the first-order ionospheric delay. Therefore, after re-parameterization, the actually estimable quantity at the service-side is no longer the absolutely unbiased first-order slant ionospheric delay I_{r}^{s}, but rather a combined quantity that absorbs the receiver-side and satellite-side GF code biases, namely:

$$\bar{I}_{r}^{s}=I_{r}^{s}+b_{r,\mathrm{GF}}-b_{\mathrm{GF}}^{s} \quad (4)$$

Correspondingly, the original carrier-phase ambiguity parameters are also re-parameterized together with the carrier-phase hardware biases and part of the code biases into new estimable ambiguity parameters. As a result, for the service-side observation equations, Eq. (1) can be further rewritten as:

$$\begin{cases} E\left(\Delta P_{r,i}^{s}\right)=\mathbf{c}_{r}^{s}\cdot\Delta\mathbf{x}_{r}+c\left(\bar{dt}_{r}-\bar{dt}^{s}\right)+g_{r}^{s}\bar{T}_{r}^{s}+\mu_{i}\bar{I}_{r}^{s}+\bar{b}_{r,i}^{s} \\ E\left(\Delta\Phi_{r,i}^{s}\right)=\mathbf{c}_{r}^{s}\cdot\Delta\mathbf{x}_{r}+c\left(\bar{dt}_{r}-\bar{dt}^{s}\right)+g_{r}^{s}\bar{T}_{r}^{s}-\mu_{i}\bar{I}_{r}^{s}+\lambda_{i}\bar{N}_{r,i}^{s} \end{cases} \quad (5)$$

where $\bar{dt}_{r}$, $\bar{dt}^{s}$, $\bar{T}_{r}^{s}$, $\bar{b}_{r,i}^{s}$ and $\bar{N}_{r,i}^{s}$ denote the re-parameterized receiver clock offset, satellite clock offset, tropospheric parameter, pseudorange bias term, and ambiguity parameter, respectively. Existing ionospheric observation extraction methods mainly include the carrier-to-code leveling (CCL) method (Ciraolo et al., 2007), undifferenced and uncombined

precise point positioning (UD-PPP) (B. Zhang et al., 2012), and integer ambiguity-fixed PPP (PPP-fixed) (Ren et al., 2020). The CCL method is relatively sensitive to pseudorange noise and is prone to inconsistency among different satellite arcs. The UD-PPP method is still limited by float ambiguity estimation in terms of ionospheric estimation accuracy. In contrast, the PPP-fixed method uses uncalibrated phase delay (UPD) products to achieve ambiguity fixing, thereby obtaining ionospheric parameters that are more stable, more accurate, and more consistent among satellites. Since the experimental analysis in this study is relatively sensitive to the accuracy of ionospheric corrections, the PPP-fixed method is adopted at the service-side to estimate $\overline{I}_r^s$ for each reference station in each satellite direction.

After obtaining the high-precision estimable ionospheric parameters at all reference stations, let the reference-station ionospheric parameter vector for satellite s be defined as:

$$\overline{\mathbf{I}}^s = \left[\overline{I}_1^s \;\; \overline{I}_2^s \;\; \cdots \;\; \overline{I}_m^s \right]^{\mathrm{T}} \tag{6}$$

where m is the number of reference stations involved in the modeling. In this study, the least-squares collocation (LSC) method is adopted to map the ionospheric parameters from the reference-station network to the user location (Moritz, 1978). Let $\mathbf{C}_{II}$ denote the covariance matrix of the reference-station ionospheric parameter vector $\overline{\mathbf{I}}^s$, and let $\mathbf{c}_{uI}$ denote the cross-covariance vector between the user location and the reference stations. Then, the regional ionospheric correction for satellite $s$at the user location can be expressed as:

$$\hat{I}_u^s = \mathbf{c}_{uI}\mathbf{C}_{II}^{-1}\overline{\mathbf{I}}^s \tag{7}$$

and the corresponding theoretical interpolation error variance is:

$$\sigma_{u,s}^2 = C_{uu} - \mathbf{c}_{uI}\mathbf{C}_{II}^{-1}\mathbf{c}_{uI}^{\mathrm{T}} \tag{8}$$

where C_{uu} is the prior variance of the ionospheric random field at the user location. Equations (7) and (8) indicate that the accuracy of the regional ionospheric correction at the user-side depends not only on the estimation quality of the reference-station ionospheric parameters themselves, but also closely on the geometry of the reference-station network and the adopted covariance model.

Accordingly, the service-side can provide the regional ionospheric correction $\hat{I}_u^s$, together with model-derived precision information characterized by Eq. (8). These quantities form the external prior information required for constructing the ionosphere-constrained PPP-RTK model at the user-side.

2.2 User-side processing

Based on the regional ionospheric correction $\hat{I}_u^s$ provided by the service-side for satellite s, together with its associated precision information $\sigma_{I,u,s}^2$, and after applying the satellite clock correction in a unified manner, the user-side ionosphere-constrained PPP-RTK model can be written as:

$$\begin{cases} E\left(\Delta P_{u,i}^s + c\overline{dt}^s - \mu_i \hat{I}_u^s\right) = \mathbf{c}_u^s \cdot \Delta\mathbf{x}_u + c\overline{dt}_u + g_u^s \overline{T}_u + \mu_i \Delta I_u^s + \overline{B}_{u,i}^s \\ E\left(\Delta \Phi_{u,i}^s + c\overline{dt}^s + \mu_i \hat{I}_u^s\right) = \mathbf{c}_u^s \cdot \Delta\mathbf{x}_u + c\overline{dt}_u + g_u^s \overline{T}_u - \mu_i \Delta I_u^s + \lambda_i \overline{N}_{u,i}^s \\ 0 = \Delta I_u^s + \varepsilon_{I,u}^s, \varepsilon_{I,u}^s \sim \mathrm{N}\left(0, \lambda_I \cdot \sigma_{I,u,s}^2\right) \end{cases} \tag{9}$$

where ΔI_u^s denotes the residual error between the true user-side ionospheric delay and the service-side correction, for which a zero-mean prior constraint is imposed. λ_I is the scaling factor that controls the strength of the user-side ionospheric constraint. A smaller λ_I indicates that the user tends to place greater confidence in the service-side correction, whereas a larger λ_I indicates a more conservative user-side strategy that allows a larger residual ionospheric bias.

To provide a unified formulation of the user-side estimation process, let the user-side state vector be denoted by $\mathbf{x}_u$:

$$\mathbf{x}_u = \left[\Delta\mathbf{x}_u^{\mathrm{T}}, \overline{dt}_u, \overline{T}_u, \Delta\mathbf{I}_u^{\mathrm{T}}, \overline{\mathbf{N}}_u^{\mathrm{T}} \right]^{\mathrm{T}} \tag{10}$$

Then, Eq. (9) can be further rearranged into the following unified matrix form:

$$\begin{bmatrix} \mathbf{v}_P \\ \mathbf{v}_\Phi \\ \mathbf{v}_I \end{bmatrix} = \begin{bmatrix} \mathbf{H}_P \\ \mathbf{H}_\Phi \\ \mathbf{H}_I \end{bmatrix} \Delta\mathbf{x}_u - \begin{bmatrix} \mathbf{l}_P \\ \mathbf{l}_\Phi \\ \mathbf{0} \end{bmatrix}, \mathbf{R} = \mathrm{blkdiag}(\mathbf{R}_P, \mathbf{R}_\Phi, \lambda_I \mathbf{Q}_I) \tag{11}$$

where $\mathbf{H}_P$, $\mathbf{H}_\Phi$, and $\mathbf{H}_I$ denote the design matrices corresponding to the pseudorange observations, carrier-phase observations, and ionospheric constraints, respectively; $\mathbf{R}_P$ and $\mathbf{R}_\Phi$ denote the covariance matrices of pseudorange and carrier-phase observation noise, respectively; and $\mathbf{Q}_I$ is constructed from the precision information of the ionospheric corrections provided by the service-side. The operator $\mathrm{blkdiag}(.)$ denotes the block-diagonal matrix construction operator.

According to different constraint strengths, the ionospheric constraint strategies can be classified into three typical categories (Zha et al., 2021):

$$\begin{cases} \text{ionosphere-fixed:} & \lambda_I \to 0 \\ \text{ionosphere-weighted:} & 0 < \lambda_I < \infty \\ \text{ionosphere-float:} & \lambda_I \to \infty \end{cases} \tag{12}$$

Among them, the ionosphere-fixed strategy is equivalent to treating the service-side ionospheric correction as an almost error-free external hard constraint, which significantly compresses the degrees of freedom of the ionospheric error and therefore is the most sensitive to the accuracy of the correction information. Under the ionosphere-float strategy, the

service-side correction plays almost no constraining role in the user-side solution, leaving more sufficient ionospheric freedom, but also imposing the highest requirement on the redundancy of the user's own observations. The ionosphere-weighted strategy lies between the two extremes and establishes a continuous adjustment mechanism between external augmentation and internal robustness. Therefore, as the number of observed constellations, frequencies, and effective observations increases, the relative advantages among different constraint strategies will be directly altered.

Figure 1 summarizes the processing flow of the PPP-RTK atmospheric augmentation approach adopted in this study. The service-side generates atmospheric delay corrections together with their quality information and broadcasts them to the user-side. According to the different levels of reliance on external product precision and observation conditions under different constraint strategies, the user-side applies the corresponding atmospheric constraint scheme to achieve PPP-RTK positioning.

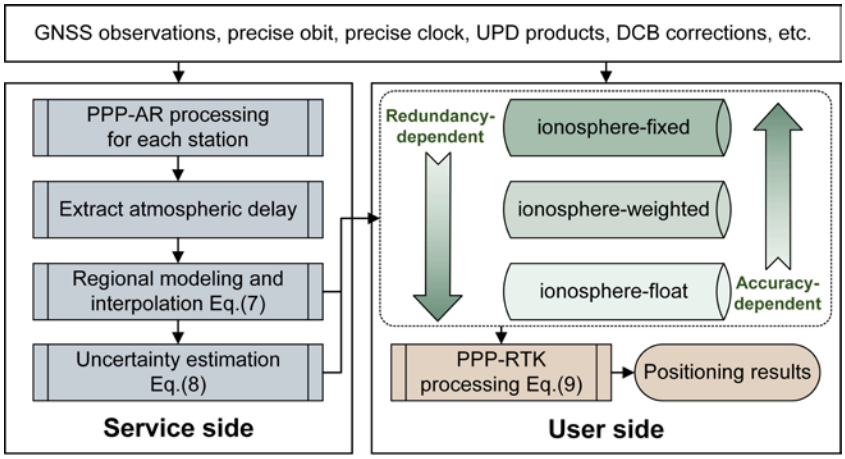

Fig. 1 Processing flow of service-side and user-side processing in PPP-RTK

3. Experimental data and processing strategies

To evaluate the adaptability of different atmospheric constraint strategies under different network spatial configurations, three reference station networks located in Australia were selected in this study, as shown in Fig. 2(a)-(c). The three networks exhibit significantly different spatial characteristics: Network 1 is a short-baseline local network; Network 2 is a regional network with relatively wide coverage; and in Network 3, the user station is located near the spatial edge of the network. These three network types are used to analyze differences in product performance under local-network, sparse-network, and edge-network conditions, respectively. The experimental observation day selected in this study is day of year (DOY) 016, 2026.

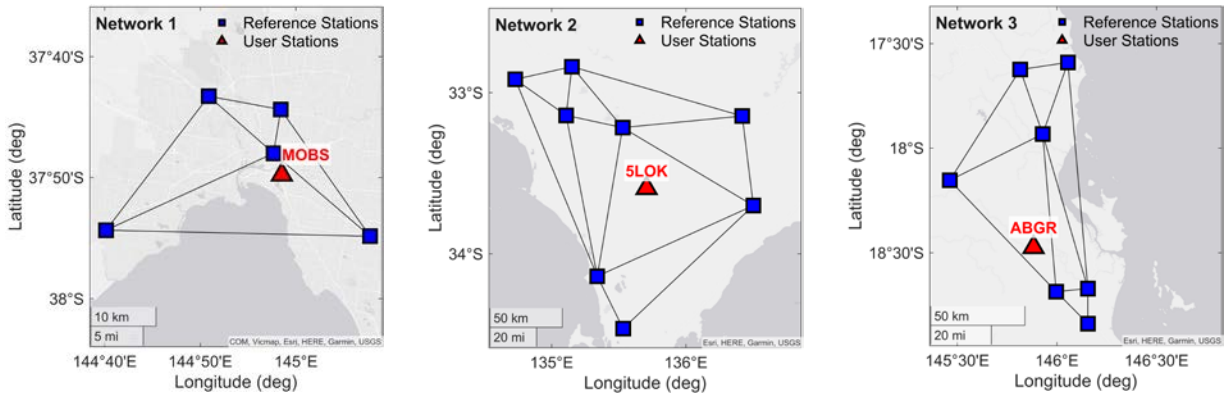

(a) (b) (c)

Fig. 2 Distribution of the reference station networks. (a) Network 1: the user station is MOBS; (b) Network 2: the user station is 5LOK; (c) Network 3: the user station is ABGR

To further characterize the ionospheric conditions of the selected test day, Fig. 3 presents the rate of total electron content index (ROTI) time series of the three user stations corresponding to the three reference-station networks. It can be seen that the three stations experienced different local ionospheric activity levels during DOY 016, 2026. In particular, MOBS was mostly associated with relatively quiet conditions, whereas 5LOK and ABGR exhibited more frequent ROTI enhancements, with some intervals exceeding 0.2 total electron content units (TECU) per minute. This provides supplementary support for comparing the behaviors of different ionospheric

constraint strategies under varying within-day ionospheric conditions.

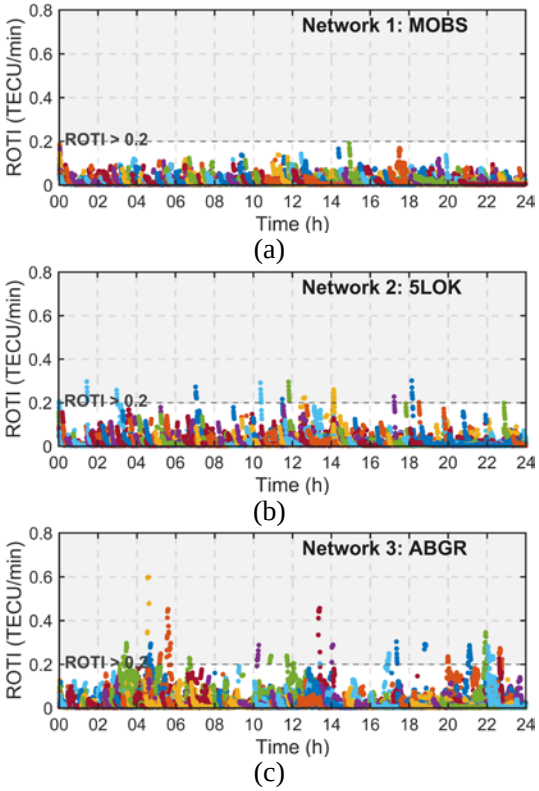

Fig. 3 Time series of ROTI at the three user stations on DOY 016, 2026. (a) Network 1: MOBS; (b) Network 2: 5LOK; (c) Network 3: ABGR

Figure 4 presents the statistics of the slant ionospheric interpolation errors based on the LSC method under the three reference-station network conditions. In this study, the ionospheric parameters estimated at the user station by precise point positioning with ambiguity resolution (PPP-AR) are taken as the reference values. The overall root mean square (RMS) shown in the figure corresponds to the statistical results of the interpolation errors for all observation periods and all visible satellites at the user station. Among the three networks, MOBS achieves an accuracy of 0.8 cm and shows the highest modeling accuracy. This short-baseline local network is supported by nearby reference stations around the user station, resulting in strong local spatial constraints; consequently, the interpolation errors of satellites from different constellations remain generally small and mostly stable. In contrast, 5LOK has an accuracy of 2.8 cm. Its network covers a relatively large area with longer inter-station distances, and the user station lacks sufficiently dense reference-station constraints in its vicinity. As a result, when the ionospheric pierce points of some satellites fall in regions with weak reference-station support, stronger extrapolation effects, or unbalanced geometric configurations, significantly larger interpolation errors are more likely to occur, corresponding to the abnormally high error values of some satellites in the figure. ABGR achieves an accuracy of 1.6 cm. Although the user station is located near the edge of the network, the inter-station distances are relatively short, and the interpolation errors of different satellites remain comparatively stable. Overall, factors such as inter-station distance, spatial configuration, and the relative position of the user station within the network jointly determine the modeling accuracy of the regional atmospheric field.

(a)

(b)

(c)

Fig. 4 Statistics of slant ionospheric interpolation errors for different satellites. (a) Network 1: MOBS; (b) Network 2: 5LOK; (c) Network 3: ABGR

Table 1 summarizes the PPP-RTK processing strategies adopted in this study. To further verify the performance differences among different atmospheric constraint strategies under multi-frequency multi-GNSS observation conditions, multi-frequency observation from the global positioning system (GPS), Galileo navigation satellite system (Galileo), and BeiDou navigation satellite system (BDS) were used. Since convergence performance directly reflects the enhancement effectiveness of PPP-RTK, the processing was restarted every 2 hour throughout DOY 016 to ensure sufficient validation. To avoid the influence of the convergence process of the UPD products on the experimental results (Ouyang et al., 2021), only the observation data after 02:00:00 on that day were used for analysis.

Table 1 PPP-RTK processing strategies

Items	Strategy
Observation	GPS: L1/L2/L5; Galileo: E1/E5a/E5b; BDS: B1/B2/B3
Interval	30 s
Cut-off angle	10°
Weight scheme	Elevation-dependent weighting (Shen et al., 2009)
Code biases	Corrected using differential signal biases from Chinese academy of sciences(CAS) (Wang et al. 2020)
Phase biases	Estimated as UPDs using a global network
Orbits and clocks	Post-processed precise products from center for orbit determination in Europe (CODE)
Ionosphere	Reference stations: undifferenced and uncombined estimation; user stations: constrained by corrections
Tropospheric	Zenith hydrostatic delay (ZHD) corrected by model (Collins & Langley, 1999); zenith wet tropospheric delay (ZWD) estimated as a parameter
AR strategy	LAMBDA method
Estimator	Kalman filter
Station displacements	Reference stations: static; user stations: kinematic

4. Results and discussion

This section experimentally analyzes the PPP-RTK positioning performance under different ionospheric constraint schemes based on the aforementioned data and processing strategies. Considering that different methods exhibit different degrees of dependence on product precision and observation redundancy, the discussion is carried out from three aspects: comparison among different constraint strategies, variations in observation conditions, and sensitivity of the ionosphere-weighted strategy.

4.1 PPP-RTK performance under different constraint strategies

As shown in Table 2, a controlled-variable comparative experiment was designed to analyze the impact of different ionospheric constraint strategies on PPP-RTK positioning performance. For the user station corresponding to each reference station network, the observation data were uniformly processed under triple-frequency GPS/Galileo/BDS observation conditions. For the three user stations, representative conservative fixed standard deviations were adopted for the ionospheric corrections according to the interpolation-error statistics under the corresponding reference-station network configurations. To empirically assess the uncertainty of the ionospheric corrections, the PPP-AR-derived ionospheric parameter at the user station was treated as an external reference. For each available satellite and epoch, the interpolation error was calculated as the difference between the LSC correction and the corresponding reference value. The RMS of these residuals over all valid satellites and epochs was used as an empirical indicator of the network-level correction uncertainty. As shown in Fig. 4, the RMS interpolation errors over all available satellites and epochs were 0.8, 2.8, and 1.6 cm for MOBS, 5LOK, and ABGR, respectively. Nominal uncertainty levels of 1, 3, and 2 cm were adopted for the three stations, respectively, to avoid assigning overly optimistic weights to the external ionospheric corrections. These values were used to construct the ionospheric correction covariance matrix $\boldsymbol{Q}_I$.

The three strategies were distinguished by the scaling factor of ionospheric constraint strength λ_I, where $\lambda_I = 1$ indicates direct use of the service-side product precision; $\lambda_I = 10^{-6}$ and $\lambda_I = 10^{6}$ approximately correspond to the ionosphere-fixed and ionosphere-float cases, respectively, so as to avoid the influence of extreme weights on numerical stability.

Table 2 Experimental settings for the PPP-RTK comparison under different ionospheric constraint strategies

Constraint strategies	Ionosphere-fixed	Ionosphere-weighted	Ionosphere-float
scaling factor λ_I	10^{-6}	1	10^{6}
Product uncertainty $\mathbf{Q}_I$	MOBS: 1cm; 5LOK: 3cm; ABGR: 2cm		
Observations	GPS /Galileo/BDS triple-frequency		

Figure 5 presents the PPP-RTK positioning error time series of the three user stations under different ionospheric constraint strategies. The most intuitive feature is the difference in positioning performance among the user stations. Specifically, the positioning errors of MOBS under all three strategies are clearly smaller than those of 5LOK and ABGR, indicating a positive correlation between ionospheric modeling accuracy and PPP-RTK positioning accuracy. When ionospheric modeling accuracy is high, external augmentation information can participate more effectively in parameter estimation and error separation, thereby yielding more stable positioning results. In contrast, when product accuracy degrades, error fluctuations and outliers under different strategies become more pronounced. This phenomenon indicates that the accuracy of atmospheric products is the foundation for the enhancement effect of constraint strategies and, to a large extent, determines the upper performance bound of user-side PPP-RTK.

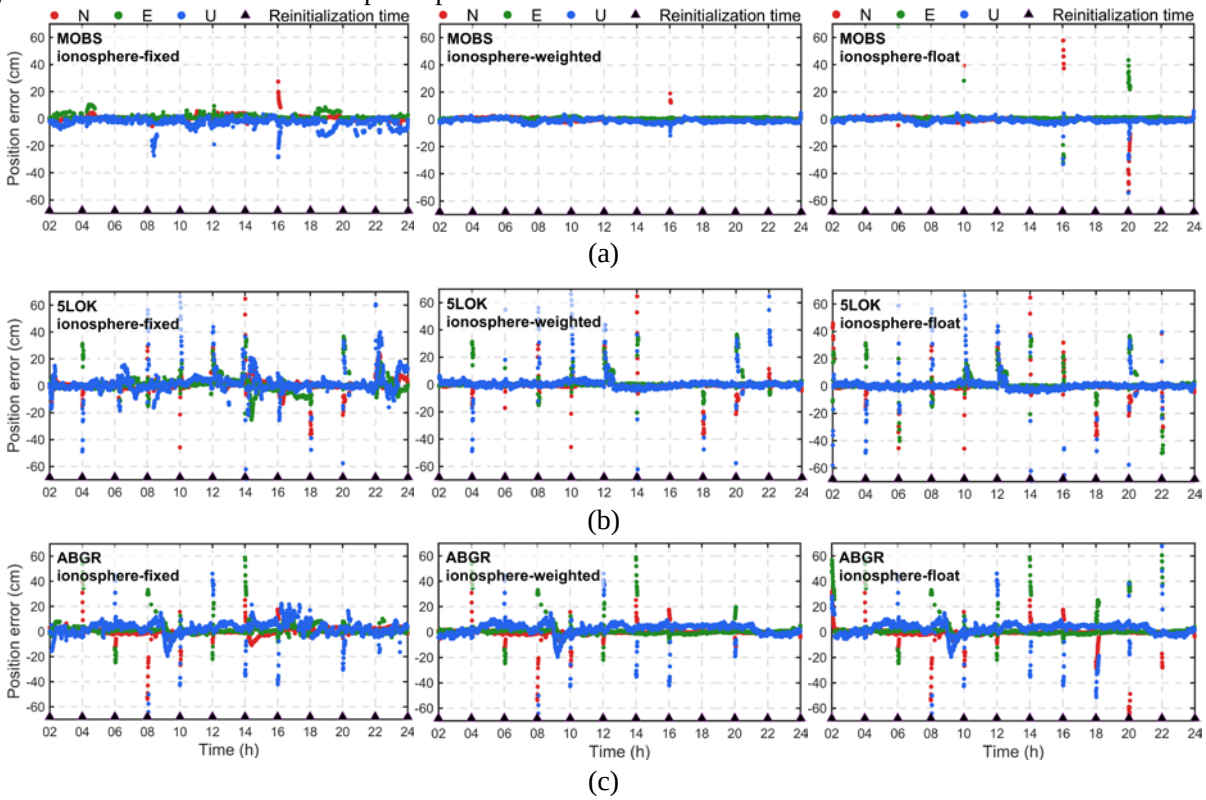

Fig. 5 PPP-RTK positioning error time series of different user stations under different ionospheric constraint strategies. (a) MOBS; (b) 5LOK; (c) ABGR

A further comparison of the positioning performance under different constraint strategies shows that all strategies exhibit certain error jumps around the restart epochs and then gradually converge to stable solutions. The differences among the strategies are mainly reflected in the convergence speed and the magnitude of anomalously high errors. Among them, the ionosphere-weighted strategy ($\lambda_I = 1$) performs the best, showing the fastest convergence and the most stable error series after convergence. The ionosphere-float strategy converges slightly more slowly, but once convergence is achieved, its positioning accuracy is generally comparable to that of the ionosphere-weighted strategy. This indicates that imposing a stochastic model constraint on atmospheric products that is consistent with their precision can significantly improve the positioning performance of PPP-RTK during the convergence stage, while maintaining relatively high solution stability after convergence. In contrast, the ionosphere-fixed strategy shows slower convergence and more pronounced abnormal deviations at multiple stations. When the actual atmospheric products still contain non-negligible modeling errors, this strategy places excessive confidence in the service-side atmospheric corrections and directly transfers product biases into the user-side solution, thereby leading to larger positioning errors.

Figure 6 further presents a statistical analysis of the above positioning results. As shown in Fig. 6(a), the ionosphere-weighted ($\lambda_I = 1$) constraint strategy

achieves the best three-dimensional positioning accuracy at all three user stations. Compared with the ionosphere-float strategy, the three-dimensional positioning error is improved by 4%-57%, while compared with the ionosphere-fixed strategy, the improvement reaches 15%-60%. Among the three stations, the accuracy differences among strategies are the most pronounced at MOBS, where the ionosphere-weighted strategy shows a more distinct advantage over the ionosphere-fixed and ionosphere-float strategies. Combined with the aforementioned ionospheric modeling accuracy, this result indicates that when the service-side product quality is high, the differences in the way external correction information is utilized by different constraint strategies are more directly reflected in the user-side positioning results.

Figure 6(b) summarizes the ambiguity fixing rates under different strategies. The ionosphere-weighted and ionosphere-float strategies exhibit relatively similar fixing rates at all user stations, and both can achieve satisfactory ambiguity fixing performance after convergence, with their differences mainly appearing during the initial convergence stage after each restart. In contrast, the ionosphere-fixed strategy yields consistently lower fixing rates at all three user stations. This again demonstrates that when residual biases still exist in the external atmospheric products, a strong constraint allows such biases to directly enter the user-side parameter estimation, thereby interfering with the separation among ionospheric, ambiguity, and position parameters in the observation model, reducing the probability of successful ambiguity fixing, and consequently degrading the overall positioning performance.

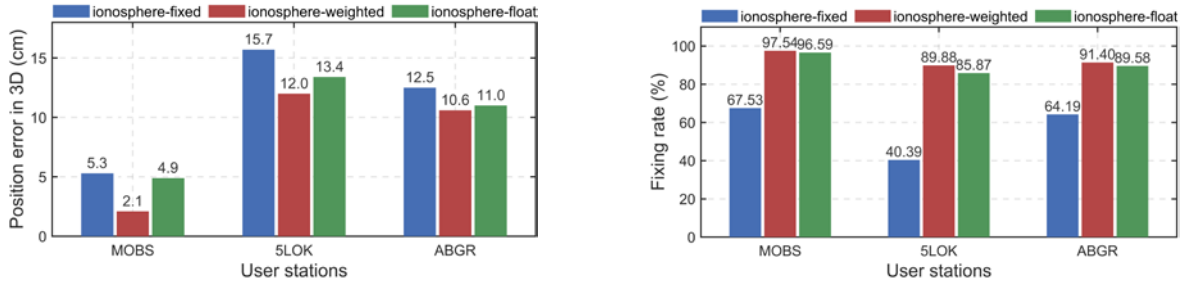

Fig. 6 Statistical results of PPP-RTK positioning performance for the three user stations under different ionospheric constraint strategies. (a) Three-dimensional positioning error; (b) ambiguity fixing rate.

4.2 PPP-RTK performance under different observation conditions

Table 3 summarizes the comparative experimental settings under different observation conditions in this section. In multi-frequency multi-GNSS PPP-RTK, the combinations of observation frequencies and constellations determine the observation redundancy of the user-side model. To analyze the impact of changes in data redundancy on PPP-RTK positioning performance, comparative experiments were designed using different combinations of frequency numbers and constellation numbers. To ensure that the control variable remains unique, and based on the experimental results obtained in the previous section, the ionosphere-weighted ($\lambda_I = 1$) constraint strategy was uniformly adopted for all user stations under all observation conditions.

Table 3 Comparative experimental settings of PPP-RTK under different observation conditions

Observations	BDS-DF	BDS-TF	BDS+GPS-TF	GPS+BDS+GAL-TF
System (frequency)	BDS (B1/B2)	BDS (B1/B2/B3)	BDS (B1/B2/B3) +GPS (L1/L2/L5)	BDS (B1/B2/B3) +GPS (L1/L2/L5) +GAL (E1/E5a/E5b)
Constraint strategies	Ionosphere-weighted			
Scaling factor λ_I	1			
Product uncertainty $\mathbf{Q}_I$	MOBS: 1cm; 5LOK: 3cm; ABGR: 2cm			

To visually illustrate the influence of different data conditions on model redundancy, Fig. 7 shows the time series of model redundancy at station MOBS under different observation conditions. The redundancy shown in the figure is defined as the difference between the number of observation equations and the number of unknown parameters at each epoch, and is used to characterize the effective degrees of freedom available for parameter separation and error absorption in the user-side positioning model. As the numbers of observed constellations and frequencies increase, the redundancy of the user positioning model also increases. The average temporal redundancies of BDS-DF, BDS-TF, BDS+GPS-TF, and BDS+GPS+GAL-TF (GAL: Galileo) are approximately 34, 39, 55, and 86,

respectively. These results indicate that, compared with increasing the number of frequencies for the same satellite system, increasing the number of observed constellations contributes more significantly to the improvement of model redundancy. This is because frequency expansion mainly adds multi-frequency observations for the same satellites, while also introducing additional inter-frequency parameters and ambiguity parameters. In contrast, constellation expansion simultaneously increases the number of independent satellites, the number of observation equations, and the strength of spatial geometric constraints, and therefore improves user-side model redundancy more directly.

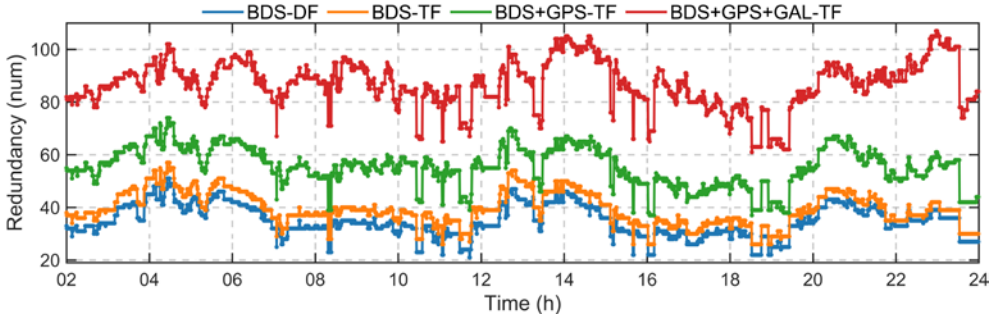

Fig. 7 Time series of PPP-RTK model redundancy at the MOBS user station under different observation conditions

As shown in Fig. 8, the horizontal and vertical positioning errors of each user station under different observation conditions are presented. Overall, under the same ionospheric constraint strategy, the positioning performance shows a generally consistent relationship with the redundancy of the user-side model: observation conditions with higher redundancy exhibit more concentrated horizontal error distributions, smaller vertical error fluctuations, and better overall positioning accuracy.

This difference is most pronounced during the convergence stage after each restart. Under observation conditions with higher redundancy, the positioning solution can usually converge to a stable level more rapidly. This indicates that higher model redundancy can provide more sufficient estimation information for the separation of position parameters, ambiguity parameters, and atmospheric parameters. Under properly imposed external atmospheric constraints, the advantages of combined multi frequency and multi-GNSS observations can be more fully exploited, thereby accelerating the convergence process of PPP-RTK.

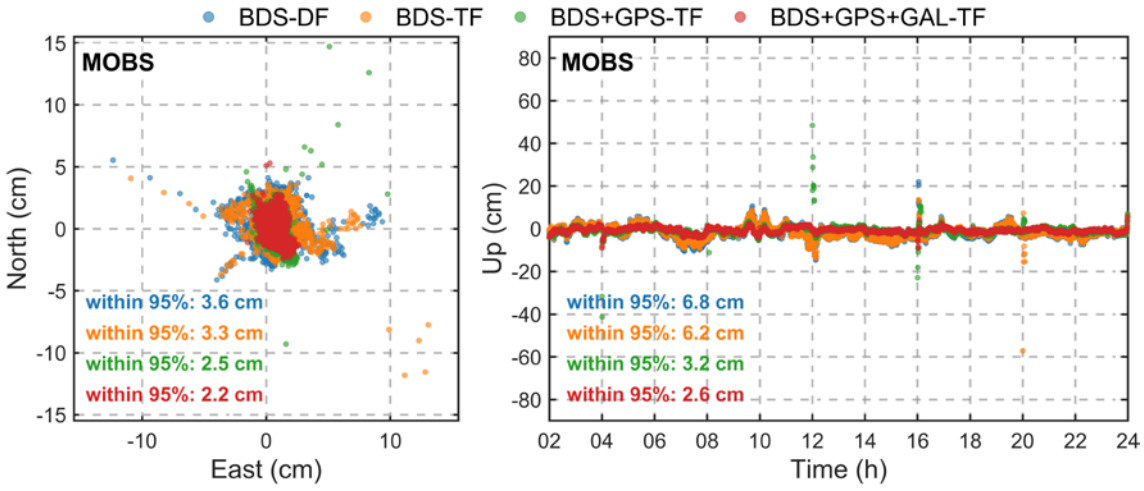

(a)

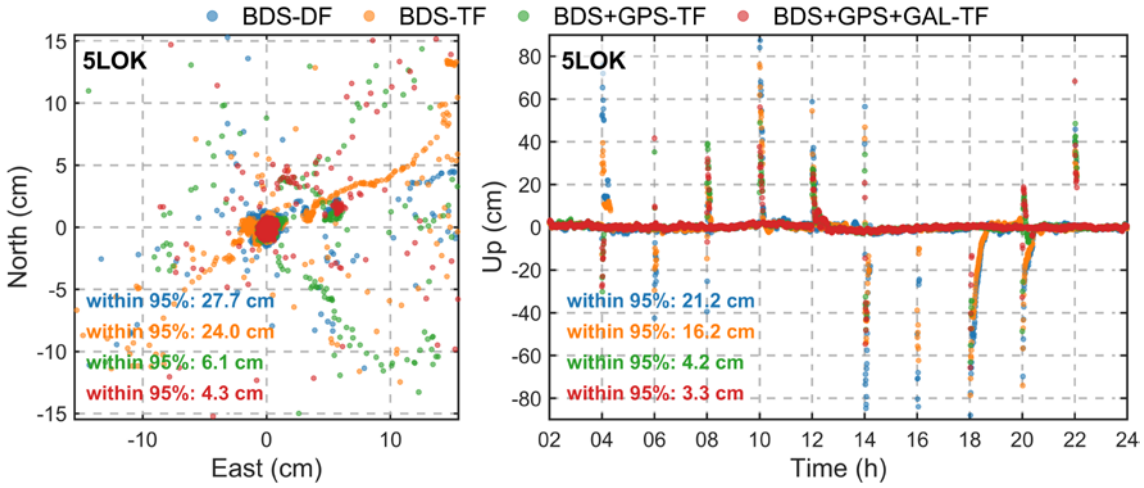

(b)

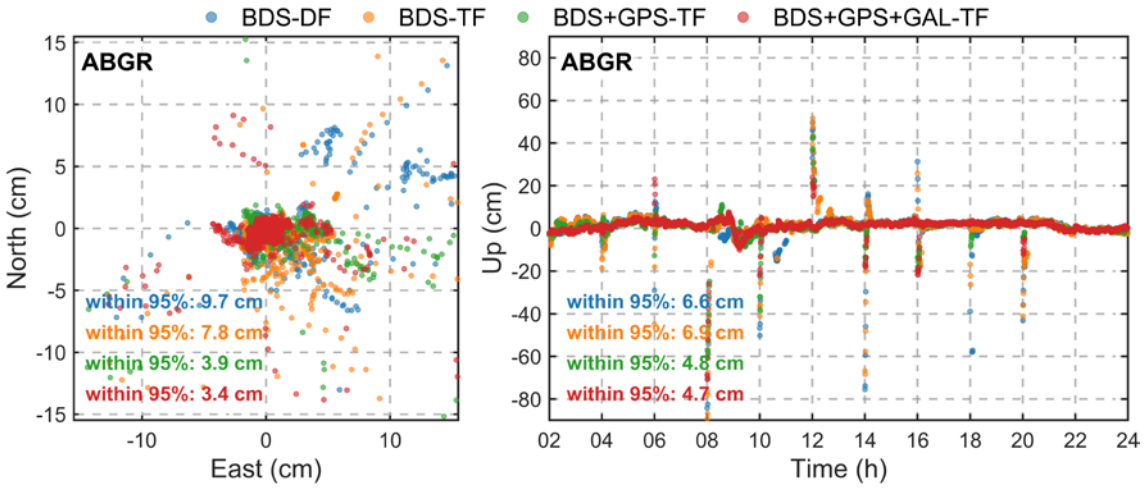

(c)

Fig. 8 Horizontal and vertical PPP-RTK positioning errors of different user stations under different observation conditions. (a) MOBS; (b) 5LOK; (c) ABGR

After reaching a stable state, observation conditions with higher model redundancy still retain certain advantages. On the one hand, higher model redundancy is beneficial for increasing the probability of detecting anomalous observations, thus providing more favorable conditions for quality control. On the other hand, when some non-significant anomalies remain undetected in the observations, a model with higher redundancy can disperse their influence on parameter estimation in the joint adjustment process, thereby mitigating the disturbance of noise and other anomalies on the positioning results.

Therefore, under the BDS+GPS+GAL-TF observation condition, the error distribution is the most compact and the abnormal fluctuations in the vertical component are the smallest, whereas the lower-redundancy BDS-DF and BDS-TF observation conditions are more prone to error divergence and abnormally large vertical errors. Overall, the increase in observation redundancy not only improves the convergence performance of PPP-RTK, but also enhances the robustness of positioning after convergence.

Table 4 further summarizes the positioning performance of each user station under different observation conditions. Overall, under the uniformly adopted ionosphere-weighted constraint strategy, BDS+GPS+GAL-TF achieves the best horizontal and vertical positioning accuracies as well as the highest ambiguity fixing rate at all three user stations.

From the perspective of the number of frequencies, under the single-constellation BDS condition, when the observation model is extended from dual-frequency to triple-frequency, the horizontal positioning error of each user station is improved by 4%-17%, while the vertical positioning error is improved by 5%-23%. This indicates that increasing the number of observation frequencies can enhance the observation redundancy within the same constellation and provide more observation information for parameter estimation, thereby improving positioning performance. However, the magnitude of this improvement remains relatively limited.

In contrast, the improvement brought by increasing the number of constellations is more

significant. When the observation model is extended from BDS+GPS-TF to BDS+GPS+GAL-TF, the horizontal positioning error of each user station is improved by 11%-46%, and the vertical positioning error is improved by 2%-41%. This result is consistent with the previous analysis of model redundancy: compared with increasing the number of observation frequencies for the same satellites, increasing the number of observed constellations can more significantly improve the redundancy and constraint strength of the positioning model, thereby enhancing the performance of ambiguity fixing and parameter estimation. Therefore, in multi-frequency multi-GNSS PPP-RTK, constellation expansion contributes more significantly than frequency expansion to the improvement of positioning accuracy and ambiguity fixing rate.

Table 4 Statistical results of PPP-RTK positioning performance for different user stations under different observation conditions

Observations	MOBS			5LOK			ABGR		
	H (cm)	U (cm)	Fixing rate (%)	H (cm)	U (cm)	Fixing rate (%)	H (cm)	U (cm)	Fixing rate (%)
BDS-DF	3.5	3.6	96.21	10.3	13.5	84.95	6.7	7.2	88.40
BDS-TF	3.2	3.4	96.63	8.5	10.4	89.61	6.4	6.7	91.33
BDS+GPS-TF	2.6	2.9	96.98	3.5	7.5	93.08	3.8	4.6	95.75
BDS+GPS+GAL-TF	1.4	1.7	97.57	3.1	6.7	95.06	3.2	4.5	96.47

4.3 Sensitivity of ionospheric-weighted constraints under different observation conditions

Based on the experimental results presented in the previous two sections, different ionospheric constraint strategies significantly affect the positioning performance of PPP-RTK. Among them, the ionosphere-weighted strategy shows better adaptability in balancing the utilization of external atmospheric products and positioning stability. Meanwhile, as the numbers of observed constellations and frequencies increase, the redundancy of the user-side model is significantly enhanced, and the convergence performance and positioning accuracy of PPP-RTK are correspondingly improved. On this basis, this section further discusses the sensitivity of the weighting scaling factor under the ionosphere-weighted strategy to different observation conditions, so as to provide an analytical basis for the rational selection of constraint strategies under different observation conditions.

Figure 9 shows the variation of ambiguity fixing rate with the scaling factor λ_I at station MOBS under different observation conditions. For all types of observation conditions, the ambiguity fixing rate approaches its highest level when the scaling factor $\lambda_I = 1$. This indicates that when the user-side adopts a stochastic constraint consistent with the precision of the service-side products, the external atmospheric correction information can be utilized most effectively. When the scaling factor deviates from 1, however, the fixing rate decreases regardless of whether the constraint is strengthened or weakened.

However, the effects of decreasing and increasing the scaling factor on the fixing rate are different. As the scaling factor λ_I gradually decreases, the fixing rate drops more rapidly. When it approaches 0, the constraint form becomes close to the ionosphere-fixed strategy, and the fixing rate correspondingly approaches the lower bound associated with the ionosphere-fixed case. By contrast, as the scaling factor λ_I gradually increases, the fixing rate decreases more slowly and gradually approaches the lower bound corresponding to ionosphere-float. The lower bound associated with ionosphere-float is, overall, significantly higher than that of ionosphere-fixed. Therefore, when residual biases remain in the atmospheric products, a moderately conservative constraint, although weakening the enhancement effect of external information, usually does not excessively degrade the ambiguity fixing performance. From the perspective of product uncertainty estimation, the variation of the scaling factor can also be interpreted as a mischaracterization of the ionospheric correction uncertainty. When $\lambda_I < 1$, the effective uncertainty assigned to the external ionospheric corrections is smaller than the nominal value, corresponding to an overconfident or underestimated uncertainty model. In this case, residual errors in the ionospheric corrections receive excessive weight and are more likely to propagate into the ambiguity and position estimates. In contrast, $\lambda_I > 1$ corresponds to a conservative overestimation of the product uncertainty. Although this weakens the contribution of the external ionospheric information, the resulting performance degradation is generally more gradual. These results indicate that underestimating the product uncertainty can be more detrimental to the ionosphere-weighted strategy than moderately overestimating it.

In addition, differences can also be observed among the curves under different observation conditions. Under high-redundancy observation conditions, the fixing-rate curves are flatter in the region of larger scaling factors, meaning that when the constraint strategy gradually becomes more conservative, the performance loss relative to the optimal level remains smaller. This indicates that under better observation conditions, the user-side model itself already possesses stronger capabilities for

parameter separation and ambiguity resolution, and is therefore less sensitive to the strength of the external atmospheric constraints. Consequently, for multi-frequency multi-GNSS PPP-RTK, under high-redundancy observation conditions, the choice of constraint strategy may be shifted moderately toward the conservative side in order to reduce the potential positioning risk caused by product biases.

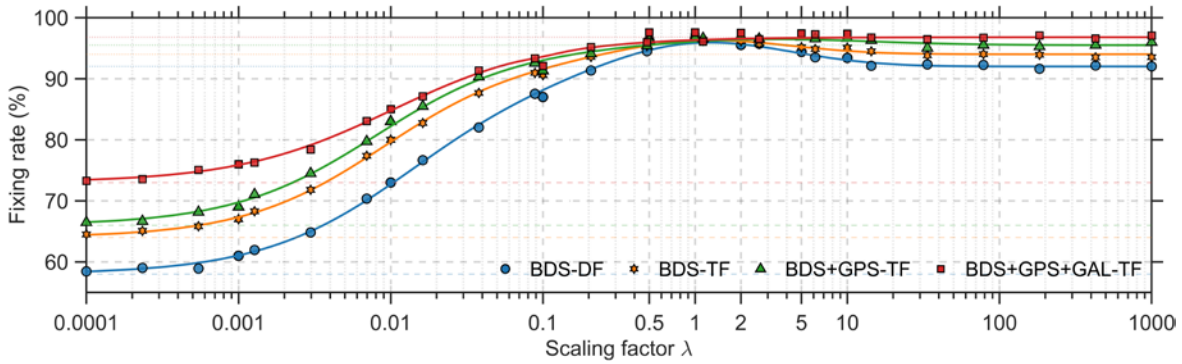

Fig. 9 Relationship between ambiguity fixing rate and the scaling factor at station MOBS under different observation conditions

Similarly, Fig. 10 shows the variation of the three-dimensional positioning error with the scaling factor, and its changing pattern is generally consistent with the ambiguity fixing rate results shown in Fig. 9. Overall, when the scaling factor $\lambda_I = 1$, the three-dimensional positioning error under all observation conditions remains close to the optimal level. For models with relatively high redundancy, such as BDS+GPS+GAL-TF, when λ_I approaches 0, the upper bound of the three-dimensional positioning error is higher than that when λ_I approaches infinity. In contrast, for the other observation conditions with relatively lower redundancy, the relative magnitudes of the error upper bounds on the left and right sides depend on the precision level of the atmospheric products corresponding to the current user station.

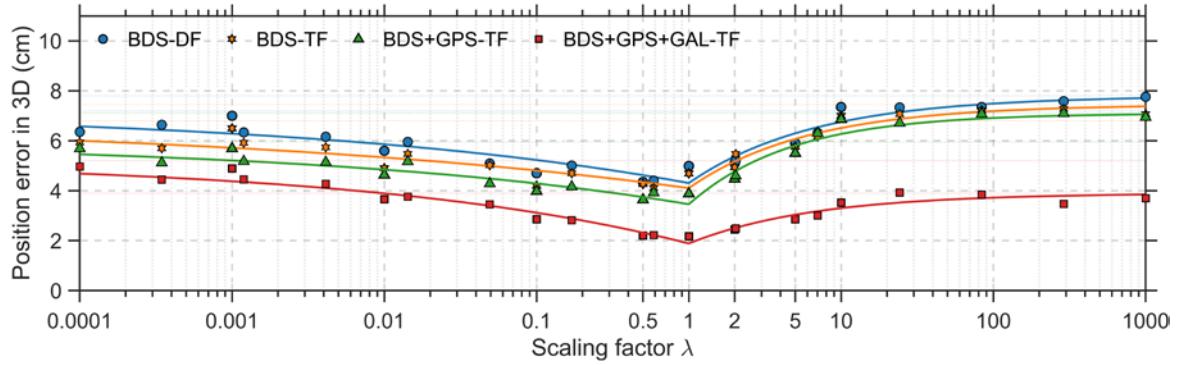

Fig. 10 Relationship between three-dimensional positioning error and the scaling factor at station MOBS under different observation conditions

The above results indicate that, as model redundancy increases, overly strong constraints make the propagation effect of product biases more pronounced, whereas the positioning performance degradation caused by conservative constraints remains relatively limited. In other words, under multi-frequency multi-GNSS PPP-RTK conditions, higher observation redundancy preserves stronger self-estimation capability for the user-side. Therefore, the selection of constraint strategies should place greater emphasis on the precision boundary of the products, rather than relying on excessively strong atmospheric constraints. More importantly, the applicability of an ionospheric constraint is jointly governed by the consistency between the assumed product uncertainty and the actual correction error, as well as by the redundancy of the user-side observation model. Therefore, the preferable constraint strength is not an intrinsic property of a particular strategy, but results from the balance between external product reliability and the user's self-estimation capability.

5. Conclusions

This study focused on the selection of ionospheric constraint strategies in multi-frequency multi- GNSS PPP-RTK. It analyzed the potential error sources and their propagation effects in the service-side ionospheric extraction and modeling process, and constructed three typical user-side PPP-RTK constraint models. It is shown that the differences among ionospheric constraint strategies are jointly governed by product precision and observation conditions, and comparative experiments were conducted accordingly. The main conclusions are as follows:

(1) Under the three network-user configurations, the ionosphere-weighted strategy achieved the best or near-best overall positioning performance among the three constraint strategies. Its three-dimensional

positioning error was reduced by 4%-57% relative to the ionosphere-float strategy and by 15%-60% relative to the ionosphere-fixed strategy. These results indicate that, for the tested product-quality levels, imposing a stochastic constraint consistent with the nominal precision of the service-side ionospheric products provided a better balance between the utilization of external augmentation information and positioning robustness.

(2) In the tested observation configurations, increasing the number of frequencies and constellations increased the redundancy of the user-side model and was accompanied by improved PPP-RTK positioning performance. When the single-constellation BDS model was extended from dual-frequency to triple-frequency, the horizontal and vertical positioning errors were reduced by 4%-17% and 5%-23%, respectively. Further extending the model from BDS+GPS-TF to BDS+GPS+GAL-TF reduced the horizontal and vertical errors by 11%-46% and 2%-41%, respectively. These results demonstrate, for the observation scenarios considered in this study, the benefit of additional multi-frequency and multi-GNSS observations for improving model redundancy and parameter-estimation stability.

(3) The ionosphere-weighted strategy achieved its best performance when the adopted constraint strength was consistent with the nominal error level of the service-side products. As the observation redundancy increased, the performance degradation caused by moderately relaxing the ionospheric constraint became smaller, indicating stronger user-side self-estimation capability under the tested multi-frequency multi-GNSS conditions. These findings suggest that the selection of constraint strength should consider both the reliability of the service-side product uncertainty and the redundancy of the user-side observation model, while overly strong constraints should be avoided when residual product biases may be present.

Declarations

Acknowledgements The authors would like to thank Geoscience Australia for providing GNSS network datasets. The precise products provided by CODE and CAS are also gratefully acknowledged.

Author contribution ZS and WG designed the research and wrote the main manuscript text. SP and QZ designed the formula and prepared Figures 1-7. XT analyzed the data and prepared Figures 8-10. All authors reviewed the manuscript.

Data availability The data that support the findings of this study are available from the corresponding author upon request.

Funding This work is partially supported by the National Natural Science Foundation of China (Grant No. 42674055) and the Fundamental Research Funds for the Central Universities of China (Grant No. 2242025RCB0023).

Competing interests The authors have no relevant financial or non-financial interests to disclose.

Consent for publication All authors have read and agreed to the published version of the manuscript.

Ethical approval Not applicable.

References

Ciraolo, L., Azpilicueta, F., Brunini, C., Meza, A., & Radicella, S. M. (2007). Calibration errors on experimental slant total electron content (TEC) determined with GPS. Journal of Geodesy, 81(2), 111–120. https://doi.org/10.1007/s00190-006-0093-1

Collins, P., & Langley, R. B. (1999). Tropospheric delay. GPS World, 53, 52–58.

Dai, L., Han, S., Wang, J., & Rizos, C. (2001). A study on GPS/GLONASS multiple reference station techniques for precise real-time carrier phase-based positioning. Proceedings of the 14th International Technical Meeting of the Satellite Division of The Institute of Navigation (ION GPS 2001), 392–403.

Du, S., Cui, B., Wang, J., Tang, L., Huang, G., & Schuh, H. (2026). Integrated ionospheric delay processing strategy for PPP-RTK: Improving uncertainty estimation accuracy and mitigating delay errors. GPS Solutions, 30(1), 12. https://doi.org/10.1007/s10291-025-01978-7

Huang, J., Li, X., Li, X., Han, J., Liang, D., & Zhang, W. (2025). Quality monitoring of grid-based atmospheric corrections in GNSS PPP-RTK service using leave-one-out cross-validation. Satellite Navigation, 6(1), 25. https://doi.org/10.1186/s43020-025-00178-5

Li, P., Cui, B., Hu, J., Liu, X., Zhang, X., Ge, M., & Schuh, H. (2022). PPP-RTK considering the ionosphere uncertainty with cross-validation. Satellite Navigation, 3(1), 10. https://doi.org/10.1186/s43020-022-00071-5

Li, X., Han, J., Li, X., Huang, J., Shen, Z., & Wu, Z. (2023). A grid-based ionospheric weighted method for PPP-RTK with diverse network scales and ionospheric activity levels. GPS Solutions, 27(4), 191. https://doi.org/10.1007/s10291-023-01522-5

Mi, X., Chen, X., Odolinski, R., Wang, Y., Chen, W., & Yuan, Y. (2026). Fast and precise GNSS RTK positioning with ionosphere-constrained weighted least squares quadratic programming. Journal of Geodesy, 100(2), 11. https://doi.org/10.1007/s00190-025-02026-5

Montenbruck, O., Hauschild, A., & Steigenberger, P. (2014). Differential code bias estimation using multi-GNSS observations and global ionosphere maps: Mulit-GNSS DCB estimation. Navigation, 61(3), 191–201. https://doi.org/10.1002/navi.64

Moritz, H. (1978). Least-squares collocation. Reviews of Geophysics, 16(3), 421–430. https://doi.org/10.1029/RG016i003p00421

Odijk, D., Van Der Marel, H., & Song, I. (2000). Precise GPS positioning by applying ionospheric corrections from an active control network. GPS Solutions, 3(3), 49–57. https://doi.org/10.1007/PL00012804

Ouyang, M., Li, J., Li, W., Ge, Y., Zhu, X., Chen, Z., & Dai, Z. (2021). Research on time and frequency transfer during PPP convergence with parameters correlation comparison. Measurement, 173, 108597. https://doi.org/10.1016/j.measurement.2020.108597

Psychas, D., & Verhagen, S. (2020). Real-time PPP-RTK performance analysis using ionospheric corrections from multi-scale network configurations. Sensors, 20(11), 3012. https://doi.org/10.3390/s20113012

Psychas, D., Verhagen, S., Liu, X., Memarzadeh, Y., & Visser, H. (2019). Assessment of ionospheric corrections for PPP-RTK using regional ionosphere modelling. Measurement Science and Technology, 30(1), 014001. https://doi.org/10.1088/1361-6501/aaefe5

Ren, X., Chen, J., Li, X., & Zhang, X. (2020). Ionospheric total electron content estimation using GNSS carrier phase observations based on zero-difference integer ambiguity: Methodology and assessment. IEEE Transactions on Geoscience and Remote Sensing, 59(1), 817–830. https://doi.org/10.1109/TGRS.2020.2989131

Shen, Y., Li, B., & Xu, G. (2009). Simplified equivalent multiple baseline solutions with elevation-dependent weights. GPS Solutions, 13(3), 165–171. https://doi.org/10.1007/s10291-008-0109-9

Song, J., Park, B., & Kee, C. (2016). Comparative analysis of height-related multiple correction interpolation methods with constraints for network RTK in mountainous areas. The Journal of Navigation, 69(5), 991–1010. https://doi.org/10.1017/S0373463316000011

Teunissen, P. J. G., & Khodabandeh, A. (2021). A mean-squared-error condition for weighting ionospheric delays in GNSS baselines. Journal of Geodesy, 95(11), 118. https://doi.org/10.1007/s00190-021-01569-7

Teunissen, P. J., Odijk, D., & Zhang, B. (2010). PPP-RTK: Results of CORS network-based PPP with integer ambiguity resolution. J Aeronaut Astronaut Aviat Ser A, 42(4), 223–230.

Wabbena, G., Schmitz, M., & Bagge, A. (2005). PPP-RTK: Precise point positioning using state-space representation in RTK networks. Proceedings of the 18th International Technical Meeting of the Satellite Division of the Institute of Navigation (ION GNSS 2005), 2584–2594.

Wang N, Li Z, Duan B, Hugentobler U, Wang L (2020) GPS and GLONASS observable-specific code bias estimation: comparison of solutions from the IGS and MGEX networks: N. Wang et al. J Geodesy 94(8):74

Wang, P., Nie, G., Liu, H., Wen, J., Wang, Y., & Shen, H. (2023). An ionosphere-weighted calibration method with multi-station network corrections. Advances in Space Research, 72(9), 3982–3997. https://doi.org/10.1016/j.asr.2023.06.057

Xiao, G., Yang, C., Wei, H., Xiao, Z., Zhou, P., Li, P., Dai, Q., Zhang, B., & Yu, C. (2024). PPP ambiguity resolution based on factor graph optimization. GPS Solutions, 28(4), 178. https://doi.org/10.1007/s10291-024-01715-6

Zha, J., Zhang, B., Liu, T., & Hou, P. (2021). Ionosphere-weighted undifferenced and uncombined PPP-RTK: Theoretical models and experimental results. GPS Solutions, 25(4), 135. https://doi.org/10.1007/s10291-021-01169-0

Zhang, B., Ou, J., Yuan, Y., & Li, Z. (2012). Extraction of line-of-sight ionospheric observables from GPS data using precise point positioning. Science China Earth Sciences, 55(11), 1919–1928. https://doi.org/10.1007/s11430-012-4454-8

Zhang, B., Teunissen, P. J., & Odijk, D. (2011). A novel un-differenced PPP-RTK concept. The Journal of Navigation, 64(S1), S180–S191. https://doi.org/10.1017/S0373463311000361

Zhang, W., Wang, J., & Khodabandeh, A. (2024). Regional ionospheric correction generation for GNSS PPP-RTK: Theoretical analyses and a new interpolation method. GPS Solutions, 28(3), 139. https://doi.org/10.1007/s10291-024-01682-y

Zhang, X., Ren, X., Chen, J., Zuo, X., Mei, D., & Liu, W. (2022). Investigating GNSS PPP–RTK with external ionospheric constraints. Satellite Navigation, 3(1), 6. https://doi.org/10.1186/s43020-022-00067-1

Zumberge, J. F., Heflin, M. B., Jefferson, D. C., Watkins, M. M., & Webb, F. H. (1997). Precise point positioning for the efficient and robust analysis of GPS data from large networks. Journal of Geophysical Research: Solid Earth, 102(B3), 5005–5017. https://doi.org/10.1029/96JB03860

Authors



Zhihan Sun is currently a Ph.D. student at the School of Instrument Science and Engineering, Southeast University, Nanjing, China. She received her B.E. degree from Southeast University in 2024. Her current research focuses on quality monitoring and quality control methods for PPP/RTK.



Wang Gao is an associate professor of Navigation, Guidance and Control at Southeast University in Nanjing,

China. He received his Ph.D. degree in 2018 from Southeast University. His current research mainly includes multi-sensors precise positioning and navigation.



Shuguo Pan is a professor of Navigation, Guidance and Control at Southeast University in Nanjing, China. He received his Ph.D. degree from Southeast University in 2007. His research interests are high-precision multi-sensors positioning and navigation control.



Qing Zhao is a postdoctoral researcher at the School of Instrument Science and Engineering, Southeast University. He received his Ph.D. degree from Southeast University in 2021. His main research interests include multi-frequency GNSS high-precision positioning algorithms and regional atmosphere modeling.



Xianlu Tao is currently a lecturer at the School of Instrument Science and Engineering, Southeast University, China. He received his B.S.C., M.S.C., and Ph.D. degrees in Geodesy and Engineering Surveying from the School of Geodesy and Geomatics of Wuhan University. His primary areas of research are GNSS high-precision positioning, multi-sensors integrated navigation, and its applications.